DOI: 10.21062/mft.2026.003 http://www.journalmt.com

Ultrasonic-Based Active Thermography for Determining Depth Detection Limits in Onyx Composites

Lucia Deganová (0009-0004-1813-4725), Vladimír Dekýš (0000-0001-5683-2058), Milan Sapieta (0000-0003-1356-1168), Alžbeta Sapietová (0000-0001-8489-0853)
Faculty of Mechanical Engineering, University of Žilina. Univerzitna 8215, 010 26 Zilina, Slovak Republic. E-mail: lucia.deganova@fstroj.uniza.sk, vladimir.dekys@fstroj.uniza.sk, milan.sapieta@fstroj.uniza.sk, alzbeta.sapietova@fstroj.uniza.sk

This paper examines the detection of internal defects in composite specimens composed of Onyx, a material featuring a nylon matrix reinforced with chopped carbon fibers. Artificial defects, in the form of flat-bottom holes of various geometries, were intentionally introduced during the additive manufacturing process. The primary objective is to determine the depth detection capabilities of ultrasound by varying the excitation frequency and determining whether these defects remain identifiable at different subsurface levels. Ultrasonic lock-in thermography is utilized to excite specimens. As the frequency is modified, the depth of wave propagation also changes, a phenomenon well established in homogeneous materials. However, the heterogeneous nature of Onyx introduces complexities into wave propagation. The recorded thermographic data are processed in MATLAB to calculate contrast ratio values, enabling a quantitative comparison of defect detectability for different defect geometries.

Keywords: Onyx composite, Ultrasonic thermography, Lock-in, Depth detection, MATLAB

1 Introduction

Recent advancements in additive manufacturing have enabled the production of advanced composite materials with customized mechanical properties. One such material is Onyx, a nylon-based (polyamide 6) thermoplastic reinforced with chopped carbon fibers, which enhances its mechanical properties, such as strength and stiffness. Onyx is a black filament with a 1.75 mm diameter, manufactured by Markforged® [1].

Onyx demonstrates a high level of tensile strength, chemical resistance, and wear performance while remaining relatively lightweight. These attributes make it suitable for various industrial applications, including aerospace, valves and fittings, wind turbine blades, and the automotive sectors, particularly for prototype parts. The raw Onyx material typically contains around 15 vol.% of short carbon fibers, with lengths ranging significantly from 35 μm to 245 μm, resulting in an average length of 105.4 μm [2]. Conversely, 3D–printed Onyx parts exhibit a reduced fiber length distribution, ranging from 7.03 μm to 44.58 μm, with approximately 10% to 20% of the volume comprised of short carbon fibers. Additionally, it was observed that the fibers are predominantly oriented in the direction of the material deposition [3].

Onyx is processed using Fused Deposition Modeling (FDM), which is a widely used and versatile additive manufacturing technique that fabricates complex structures by extruding thermoplastic polymers through a heated nozzle onto a build platform. It enables rapid prototyping and custom fabrication across various industries, including aerospace, automotive, biomedical engineering, and electronics. These applications require thermally stable materials and mechanical performance. With the growing use of FDM technology, there is an increasing need to understand the thermal behaviour of polymeric materials fabricated by this method. The effective use of 3D-printed parts in real-world applications requires a profound knowledge of how various factors, such as material composition, infill patterns, and post-processing techniques, influence their thermal behavior. In this context, non-destructive testing is becoming increasingly vital, as it provides insight into the presence of hidden flaws and allows for a more accurate prediction of service life and operational safety of the printed components [4, 5].

As noted by Ganesan, D. et al., the fabrication of Onyx composites through the FDM method may lead to defect formation, such as delamination, porosity, voids, or cracks. The increasing use of Onyx in functional and load-bearing components underscores the necessity for effective quality control and defect detection methods. Non-destructive testing (NDT) represents a form of quality assurance in modern industry, enabling the detection of defects in material without causing physical, chemical, or thermal damage to the tested components. One particularly effective NDT technique for identifying surface and subsurface defects is infrared thermography, which provides fast and contactless inspection. A subtype of this method, active thermography, involves the use of external excitation to generate a thermal response from the tested subject. Different types of excitation sources (optical and mechanical) can be employed, depending on the material properties, such as magnetic properties, surface structure, and inspectional goals.

2 State of the art

Ultrasonic thermography is an active thermography technique that transforms mechanical energy into thermal energy through friction. This process generates heat primarily at the defect interfaces, resulting in temperature variations on the surface of the specimen. These variations contrast with the uniform temperature of the intact areas, allowing defects to be identified using an infrared camera. This method has been effectively demonstrated in the detection and quantification of delamination within composite structures, including Carbon Fiber-Reinforced Polymers (CFRP) [6, 7, 8]. Additionally, it has shown considerable success in identifying sub-surface defects at depths up to 3.5 mm, which would typically be inaccessible by optical excitation methods [9].

Aerospace applications have strongly influenced the development of active infrared thermography, where it has been applied to CFRP, GFRP (Glass Fiber-Reinforced Polymer), and hybrid laminates. Ciampa, F. et al. provided a comprehensive review of applications of pulsed, lock-in, step-heating excitation methods and ultrasonic infrared thermography, emphasizing their strengths and limitations [10].

Many studies dealing with additively manufactured materials, such as PLA and ABS, have employed active thermography with optical excitation sources [11]. Metz, Ch. et al. compared flash and pulsed techniques for quality assurance of these 3D printed materials [12]. Similarly, Sapieta, M. et al. tested PLA specimens with flat-bottom holes using the lock-in principle with optical excitation provided by halogen lamps [13]. Pisonero, J. et al also used the optical lock-in principle to test artificial defects in 3D printed PLA and Nylon specimens [14].

Multiple authors described the use of various active thermography approaches in detecting defects in composites, including ultrasonic, radiographic, and eddy current testing, but their work was limited to CFRP and GFRP materials [15, 16, 17].

Loganathan et al. examined a polymer composite reinforced with randomly oriented fibers, which bears structural similarities to Onyx due to the short-fiber reinforcement, although in their case, the fibers were organic in nature. Their study was focused on ultrasonic and infrared testing methods. Vavilov et al. compared the capabilities of infrared active thermography, laser vibrometry, and laser ultrasonic inspection for defect detection in graphite/epoxy specimens. At the same time, Swiderski applied ultrasonic infrared thermography to assess impact damage in multilayer aramid composites [18, 19, 20, 21].

Beyond qualitative assessment of defect visibility, a quantitative approach has also been proposed to estimate defect depth from thermographic measurements. Moskovchenko, A. et al. investigated 3D-printed PLA specimens containing artificial defects. In their work, advanced post-processing techniques were applied, including a nonlinear fitting algorithm and Thermographic Signal Reconstruction (TSR) [22].

Based on previous studies, various active thermography techniques, including ultrasonic lock-in thermography, have been successfully applied to different types of composite materials, including polymers reinforced with carbon fibers. However, none of these studies have addressed Onyx, a short carbon-fiber reinforced nylon produced by FDM. The present study, therefore, fills this gap by evaluating Onyx specimens using ultrasonic infrared thermography under the lock-in principle and by providing practical guidelines regarding experimental parameters such as acquisition periods, sonotrode positioning, and excitation frequencies that influence defect detectability.

3 Ultrasonic lock-in thermography

The lock-in method is a specific type of Fourier Transform. In the context of classical transformation, the number of samples and sampling frequency are utilized to determine the minimum frequency of the Fourier series. This minimum frequency is the same as the f_{Lockin} frequency for the lock-in method. It is assumed that the load modulated by f_{Lockin} stimulates the system, and the harmonic function with the same frequency f_{Lockin}, amplitude A, and phase shift φ adequately describes the system's response $s(t)$ [23].

$$s(t) = Asin(2\pi f_{Lockin}t + \varphi) = \alpha\cos(2\pi f_{Lockin}t) + bsin(2\pi f_{Lockin}t) \tag{1}$$

$$\alpha = Asin(\varphi), b = Acos(\varphi) \tag{2}$$

Considering that this response's amplitude, $s(t)$, is relatively modest, and that the signal $S(t)$ being monitored likewise has a significantly larger noise level, $N(t)$, the relationship:

$$\begin{aligned} S(t) &= \frac{A_0}{2} + \sum_{k=1}^{\infty} A_k \sin(2\pi k f_{Lockin} t + \varphi_k) = \\ &= A_1 \sin(2\pi f_{Lockin} t + \varphi_1) + \left[\frac{A_0}{2} + \sum_{k=2}^{\infty} A_k \sin\,(2\pi k f_{Lockin} t + \varphi_k\right] \\ &= s(t) + N(t) \end{aligned} \tag{3}$$

If $A = A_1$ and $\varphi = \varphi_1$, then the coefficients a, b in equation (2) could be estimated by using the relationship of the Discrete Fourier transformation.

$$\alpha = \sum_{i=0}^{N-1} S_i \cos(2\pi k f_{Lockin} \Delta t)\,, \quad b = \sum_{i=0}^{N-1} S_i \sin\,(2\pi k f_{Lockin} \Delta t) \tag{4}$$

Where:

S_i…The infrared camera's i-th frame (the frames are identified by numbers from 0 to N-1),

t…The camera's frame frequency period.

For f_{Lockin}, the real and imaginary parts of *s* were calculated using a, b the amplitude *A*, and the phase φ. The phase refers to the phase shift between the response (which is a periodic local temperature variation) and the reference excitation signal. Unlike the amplitude image, which can be influenced by factors such as variations in emissivity value, reflected radiation from the object's surface, and uneven local distribution of the applied thermal wave, the phase image remains unaffected by these variables [24, 25]. In thermographic measurements, accurately determining or knowing the emissivity of the material being tested is often critical [26]. However, this parameter can be difficult to define precisely, especially for composite materials such as Onyx. Lock-in thermography addresses this challenge by utilizing phase images, which are insensitive to emissivity values. This is because the phase shift is primarily dependent on the material's thermal properties, such as its thermal diffusivity, rather than its surface emissivity. In many cases, this statement holds true, and phase images provide a clear, high-contrast representation of subsurface defects; however, when the inspected object has a highly reflective surface, distortions may occur, leading to unreadable or misleading signals.

4 Specimen preparation

The specimens used in this study were fabricated using a Markforged Mark Two 3D printer, employing the Fused Deposition Modeling (FDM) technique. In this process, the material is deposited layer by layer through a heated nozzle.

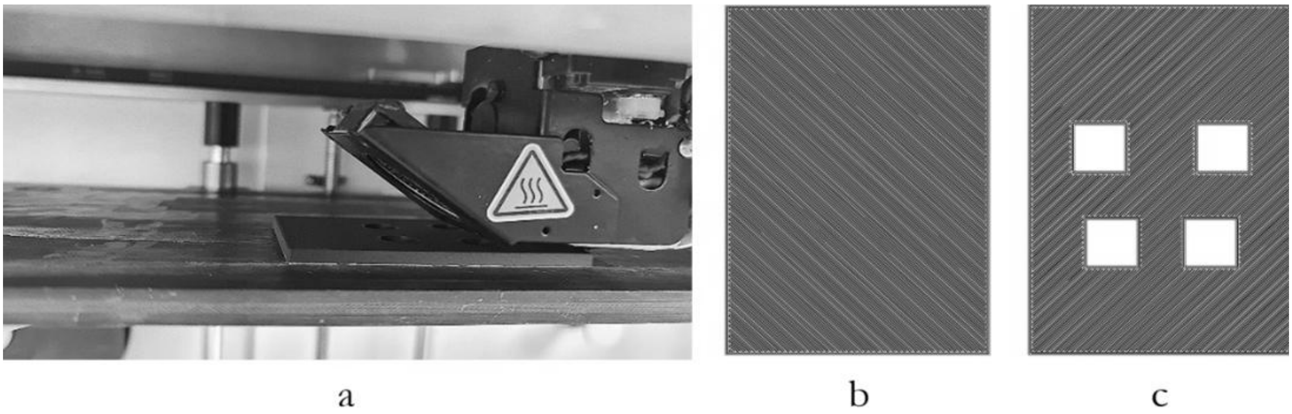

Fig. 1 *a) FDM printing of the specimen with circular flat-bottom holes; b) Bottom layer of the specimen; c) Top layer of the specimen with square flat-bottom holes*

Two types of specimens with identical dimensions were designed, differing specifically by the presence of artificially introduced defects. These defects were in the form of flat-bottom holes and were integrated directly during the additive manufacturing process. For the fabrication of these specimens, pure Onyx material was used without additional continuous fiber reinforcement. The printing parameters used for the fabrication of the specimens were as follows:

Tab. 1 *Printing parameters of the specimens*

Layer thickness [mm]	0.10
Infill density [%]	100
Number of perimeter walls	2
Total number of laminas	40
Number of top/bottom solid layers	4

The specimens were printed using a layer thickness of 0.10 mm. A fully solid infill (100% infill density) was applied, and two perimeter walls were used around the outer contour of each part. A total of 40 laminas were deposited, and four solid layers were included at both the top and bottom surfaces.

Each specimen contained four flat-bottom defects located at depths of 1 mm, 1.5 mm, 2 mm, and 3 mm beneath the inspected surface. In one specimen, the defects were circular with a radius of 10 mm, whereas in the other specimen, the defects were square-shaped with a side length of 10 mm. Both types of specimens had identical external dimensions of 54 x 78 mm and a uniform thickness of 4 mm.

The primary goal of this experiment was to investigate the ultrasonic response of the artificially created flat-bottom defects. Using variable infill percentages would introduce internal air gaps, which negatively influence the ultrasonic excitation, generating significant noise in the resulting thermograms, thereby hindering the clear identification and quantitative classification of the designed defects.

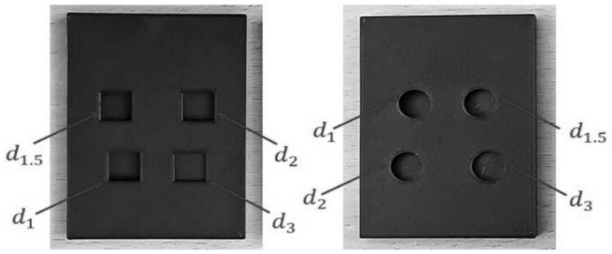

Fig. 2 *Onyx specimens with artifically introduced flat-bottom holes: circular (left) and square (right)*

The defects are visible on one side of the specimen, while the opposite side remains intact. This intact surface was used as the inspected side during thermographic measurements. In accordance with the manufacturer's specifications for the Markforged composite printing, dimensional tolerances of ±0.25% (or ±250 μm) in the X-Y plane and ±0.10% (or ±100 μm) in the Z-direction were applied to all nominal dimensions. These tolerances values were obtained from the official Markforged dimensional accuracy guidelines for the printer used to fabricate the specimens.

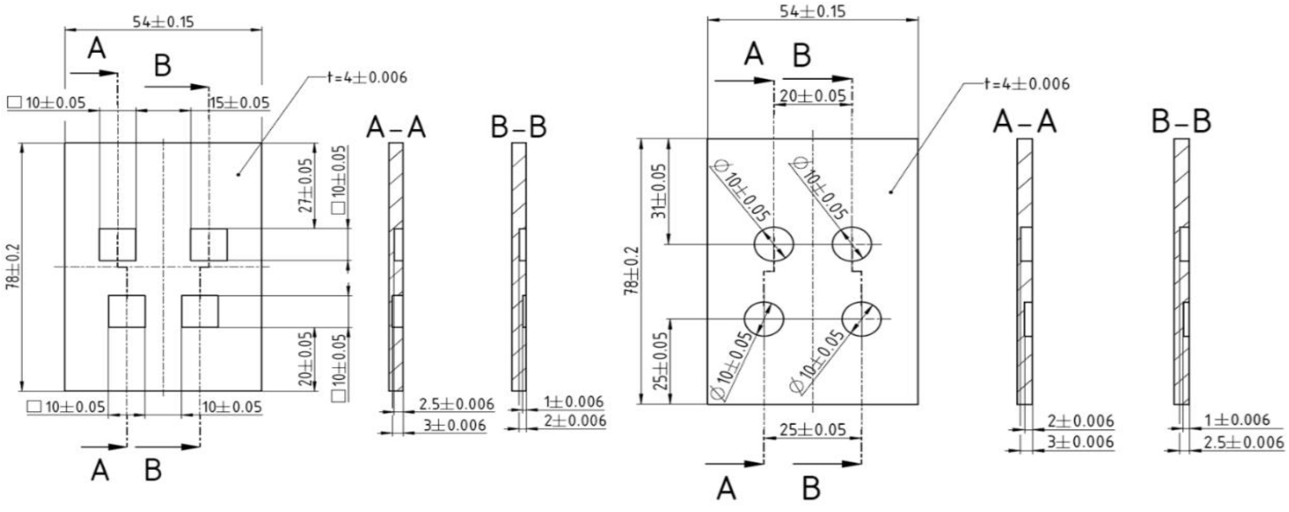

Fig. 3 *Technical drawings of the Onyx specimens showing dimensions and positions of artificially introduced flat-bottom defects (circular and square)*

5 Methodology

The experimental setup consisted of a FLIR SC7000 infrared (IR) camera operating within the mid-wave infrared (MWIR) spectral range. This camera is equipped with an actively cooled detector and offers a resolution of 320 x 256 pixels. For this experiment, a 25 mm lens was used without any filters, and the thermal response of the specimen was recorded at a frame rate of 10 Hz. The laboratory temperature was maintained at 23 °C with a relative humidity of approximately 40%.

To excite the specimen, a UTvis ultrasonic system from Edevis® GmbH was utilized. This contact-based non-destructive method involves the application of a sonotrode to the test specimen using pneumatic pressure.

The sonotrode generates high-frequency ultrasonic waves in the range of 15–25 kHz, which are modulated by a low-frequency lock-in signal f_{Lockin}. The maximum power output of the UTvis system is 2.2 kW. A specimen's surface without defects was excited, and the response to this excitation was monitored by the IR camera. A thin layer of ultrasound coupling medium (water-based lubricating gel) was applied between the sonotrode and the specimen surface to ensure efficient transmission of ultrasonic energy by eliminating air gaps that would otherwise cause acoustic impedance mismatch and reflection losses.

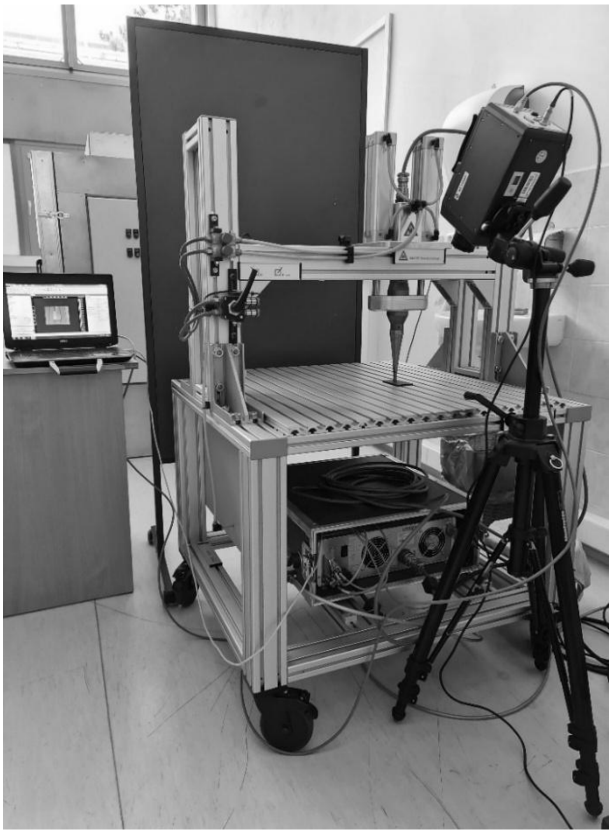

Fig. 4 *Experimental setup for ultrasonic active thermography: overall view of the measurement system with an IR camera connected to a PC and the UTvis system*

Fig. 5 *Detail of the tested specimen placed under the sonotrode, showing the intact surface*

Both the UTvis system and the IR camera were controlled using Edevis software running on a laptop. The excitation signal was sinusoidal. During the measurements, the ultrasonic frequency, amplitude, and acquisition periods were kept constant. The only varied parameter was the modulation frequency. The input parameters were set in the software as follows:

Tab. 2 *Input measurement parameters*

Ultrasound frequency	22 000 Hz
Amplitude	10%
Modulation frequency	0.1 – 0.01 Hz (varied)
Acquisition periods	2

Data acquisition and recording were conducted using the Display software provided by Edevis, with modulation frequency values being incrementally adjusted. The frequency varied in steps of 0.02 Hz within the range from 0.1 Hz to 0.01 Hz. A total of three identical specimens were printed for each geometric variant (circular and square flat-bottom defects). Since the UTvis system is primarily utilized for non-homogeneity detection in metals, it was crucial to first establish the method's feasibility for the polymer-matrix composite and subsequently optimize the input parameters. The active ultrasonic excitation combined with the lock-in technique involves a periodic ultrasonic excitation of the specimen. The primary goal of testing three specimens was to determine the optimum excitation periods, establish the threshold detection depth, and ensure the procedure remained non-destructive.

Preliminary testing revealed that an excessive number of excitation periods led to surface degradation of the specimens due to the accumulation of dissipated power and subsequent localized heating. Consequently, based on these trials, two acquisition periods were determined to be the optimal number for specimens of this thickness and geometry, successfully achieving the best defect visibility without causing material damage.

The output of the measurements included amplitude, phase, and complex images. Figures 5 and 6 display the specimens excited at a frequency of 0.02 Hz, along with a comparison of the acquired data. During the experiment, the position of the sonotrode was altered (located at the top right corner of the specimen and centred at the top) to assess how placement influenced defect detectability.

During the measurements, three types of output images were obtained: amplitude, phase, and complex. The amplitude image represents the magnitude of the thermal response to ultrasonic excitation; however, it is influenced by surface properties such as the emissivity and reflectivity of the surface. The phase image expresses the phase shift between the excitation signal and the thermal response of the specimen. Since the phase is much less affected by surface variations, it is considered more robust for evaluating subsurface defects. The complex image combines both amplitude and phase into a single representation, which can be useful for advanced data processing but is less straightforward for direct visual interpretation. For this reason, the subsequent evaluation in this study was focused primarily on phase images [27].

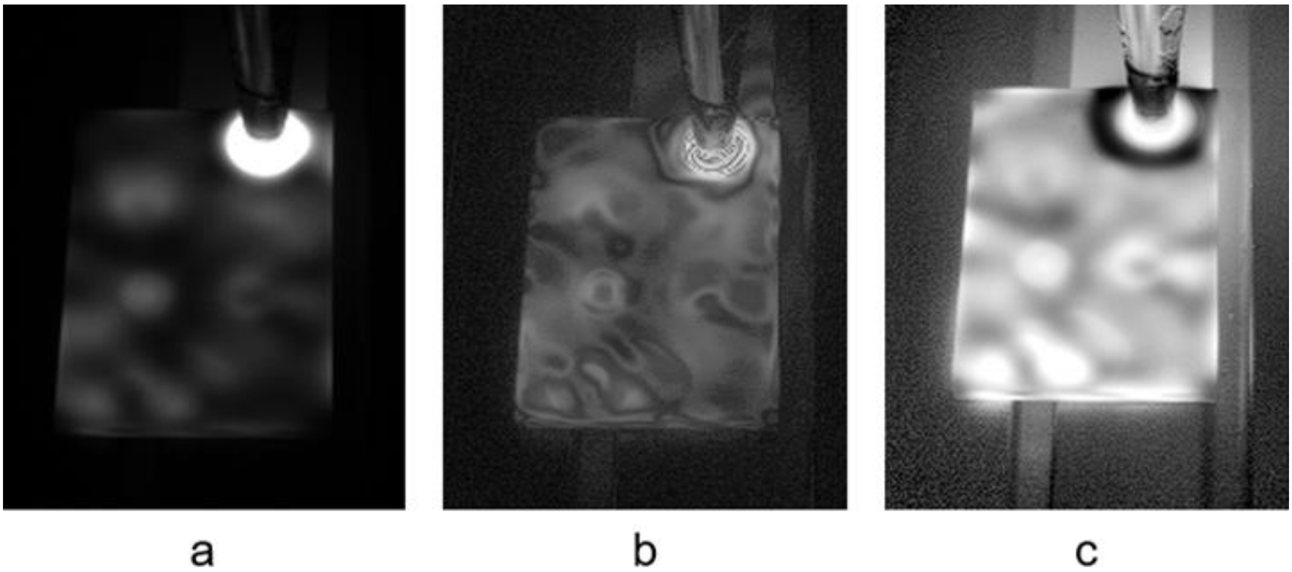

Fig. 6 *Specimen with circular flat bottom holes, frequency 0.02 Hz; a) amplitude image, b) complex image, c) phase image*

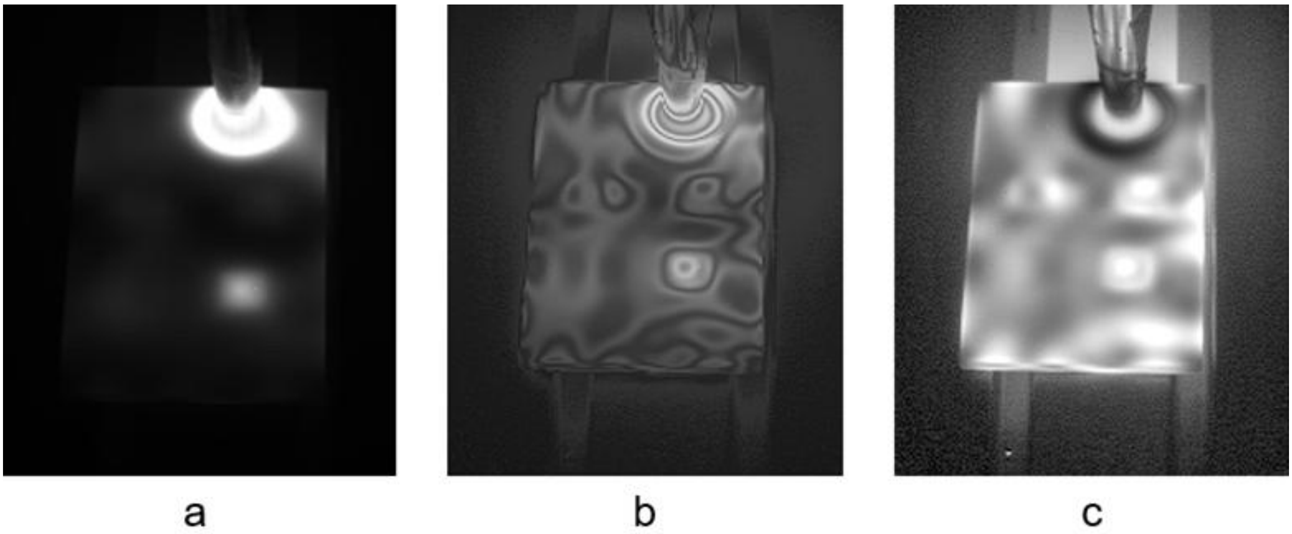

Fig. 7 *Specimen with square flat bottom holes, frequency 0.02 Hz; a) amplitude image, b) complex image, c) phase image*

The phase images were subsequently processed in MATLAB, while the images presented here serve only as a demonstration of the typical outputs obtained from ultrasonic thermography. All images were exported directly from the UTvis software without any additional modifications, representing raw measurement data.

6 Results and Discussion

The experimental results demonstrated that the placement of the ultrasonic sonotrode had a substantial impact on defect detectability. When the sonotrode was positioned at the edge of the specimen (Figure 7a), the outlines and circular shapes of two flat-bottom holes (highlighted in the red rectangle) are clearly detectable in a phase image. This visibility can be attributed to the superposition of waves, which occurs as mechanical waves reflect off the specimen boundaries. The resulting interference patterns create more complex and varied deformation gradients within the material, making the thermal anomalies caused by defects more apparent. Conversely, when the sonotrode was placed at the center of the specimen (Figure 7b), only one defect remained distinguishable. This is likely due to the highly symmetric excitation patterns, which limit the generation of complex wave interference and result in a more uniform energy distribution throughout the material. This more uniform field makes the subtle thermal signatures of defects much more difficult to detect.

In the phase images, defect resolution and detectability were assessed as a function of the applied modulation frequency, which ranged from 0.1 Hz to 0.01 Hz in increments of 0.02 Hz. The results indicate that the defect located nearest to the surface (a 3 mm deep defect situated 1 mm below the surface of the 4 mm thick specimen) was detectable at all frequencies tested, regardless of defect geometry, as can be seen in Figure 8 and Figure 9.

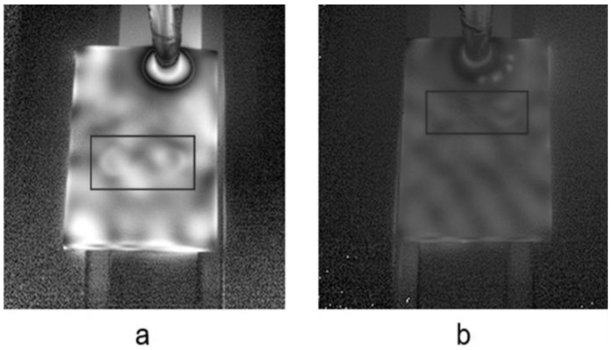

Fig. 8 *Specimen with circular flat bottom holes, frequency 0.04 Hz; a) sonotrode placement at the edge, b) sonotrode placement in the center*

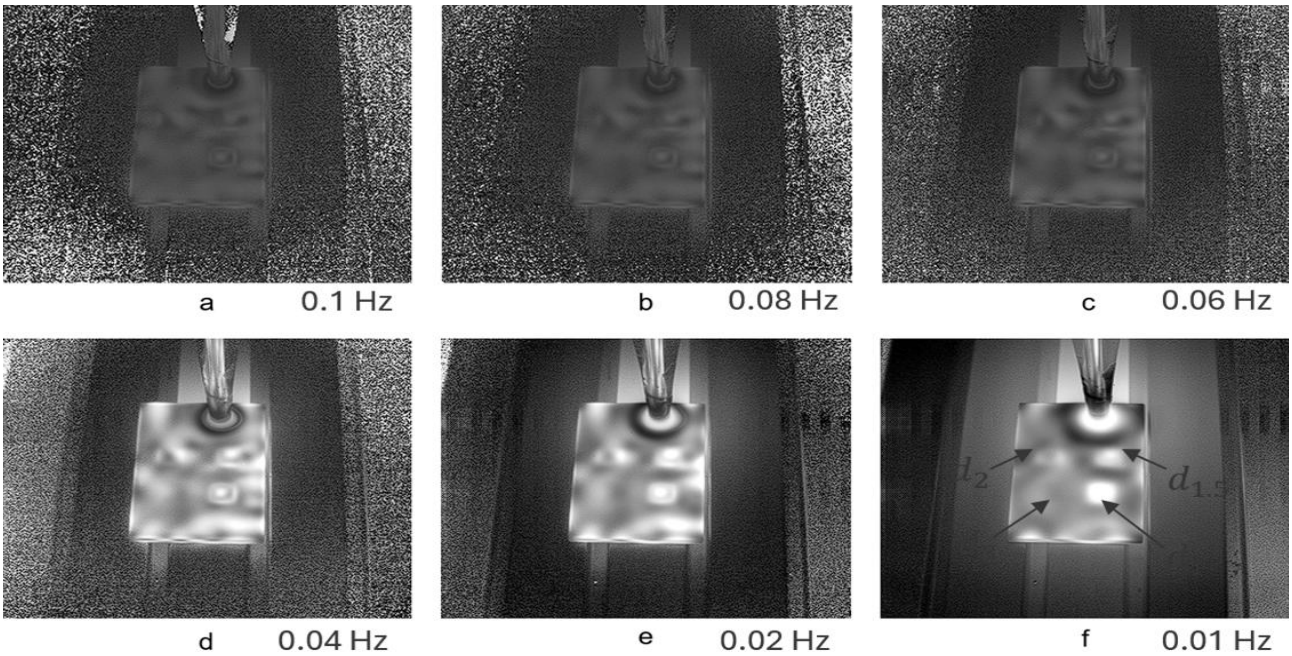

Fig. 9 *Specimen with square flat-bottom holes at various frequency values*

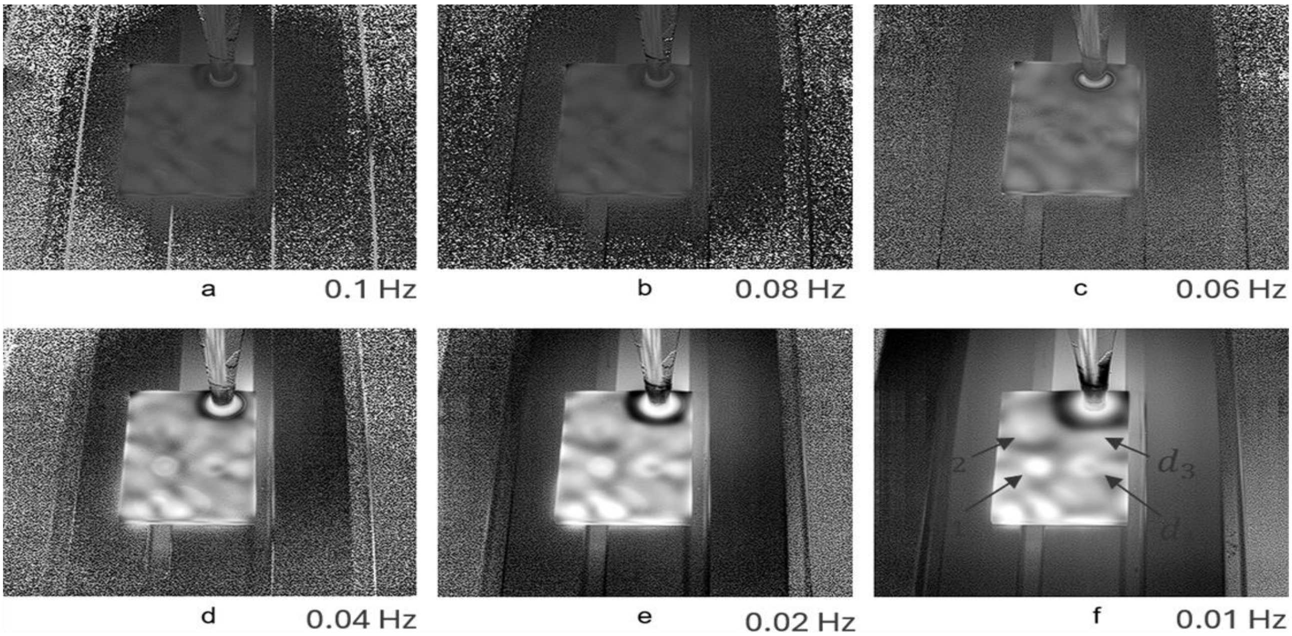

Fig. 10 *Specimen with circular flat-bottom holes at various frequency values*

Defects positioned at depths of 1.5 mm and 2 mm beneath the surface were visible only at certain frequencies. Square-shaped defects demonstrated improved visibility compared to circular ones, and a frequency of 0.04 Hz appeared to be the optimal frequency for their detection in this material. Conversely, the deepest defect, located at 3 mm below the surface, remained undetectable at all excitation frequencies examined.

An analysis of the frequency influence confirmed that lower frequencies (e.g., 0.01 Hz) facilitate greater penetration depths μ within the material, following the relationship:

$$\mu = \sqrt{\frac{\alpha}{\pi f}} \tag{5}$$

Where:

μ…The thermal diffusion length, the maximum characteristic depth to which a thermal wave can propagate into the material at a given modulation frequency [m],

α…The thermal diffusivity of the material [m^2/s],

f…The modulation frequency of the excitation [Hz],

π…Ludolf's number ≈ 3.14159.

Lower modulation frequencies enable the exploration of deeper subsurface regions, whereas higher frequencies restrict the inspection to areas closer to the surface. At higher frequencies (e.g., 0.1 Hz), enhanced resolution was achieved for defects situated near the surface, although a significantly higher level of noise accompanied the signal. This increased noise can be explained by the fact that, according to the relation:

$$T = \frac{1}{f} \tag{6}$$

Where:

T…The excitation period [s],

f…The modulation frequency [Hz].

The infrared camera has a shorter integration time at higher frequencies, which reduces its ability to average and smooth the signal. Conversely, at lower frequencies, the period is longer, allowing the acquisition system to collect more data points over each cycle, resulting in improved averaging and reduced noise. However, the reduction of frequency is also associated with a deeper penetration of the thermal wave into the material, governed by the thermal diffusivity. As a result, deeper defects can be detected, but the propagation of the thermal wave also leads to spatial blurring: the shape and edges of shallow defects, while still visible, become less sharp and well-defined due to the diffusion spreading of the thermal field.

Moreover, a notable difference in detectability was found depending on the geometry of the defects, with square-shaped defects exhibiting greater contrast than circular ones. This phenomenon can be attributed to the sharp edges and corners of square defects, which create local stress concentrations and, consequently, generate more intense frictional heating at the interface between the defect zone and the intact area of the material.

For the quantitative evaluation of defect visibility, a Contrast-to-Noise Ratio (CNR) approach was applied in the MATLAB environment. The CNR is a metric that compares the intensity difference between a defect region and its surrounding background while simultaneously normalizing this difference with respect to the noise level. In this study, the CNR was calculated using the following relation:

$$CNR = \frac{|\mu_D - \mu_B|}{\sqrt{\sigma_D^2 + \sigma_B^2}} \tag{7}$$

Where:

μ_D and μ_B…The mean pixel intensities within the defect region of interest (ROI) and the background ROI, respectively,

σ_D^2 and σ_B^2 …The corresponding standard deviations of the pixel intensities.

As the first step, a reference image at 0.04 Hz was selected, since defects appeared most clearly visible at this modulation frequency from a visual inspection perspective. Subsequently, circular or square ROIs were drawn interactively around the defects, together with rectangular background ROIs. During the ROI selection, the software displayed the size of the drawn shapes to ensure consistency across all defects. To achieve a reliable CNR calculation, the area of the background ROI was always maintained at least 1.5 times larger than the defect ROI. The position of the ROIs was then saved as binary masks and propagated across all modulation frequencies, ensuring that the same regions were consistently evaluated. This approach allowed a direct comparison of CNR values as a function of frequency.

To further validate the method, the standard deviation of CNR values was determined by introducing small artificial shifts of the background ROIs (±2 pixels in both x and y directions), while the defect ROI remained fixed. This procedure was repeated for four shifted positions in addition to the original placement, and the standard deviation of the resulting CNR values was calculated. The obtained values are presented as error bars in the graphs, indicating the sensitivity of the results to the choice of background. Larger error bars, therefore, represent frequencies where the background selection has a strong influence on the visibility of the defect, whereas smaller error bars indicate stable and reliable CNR estimates.

Figure 12 shows the dependence of the CNR on the modulation frequency for square-shaped defects located at different depths below the sample surface.

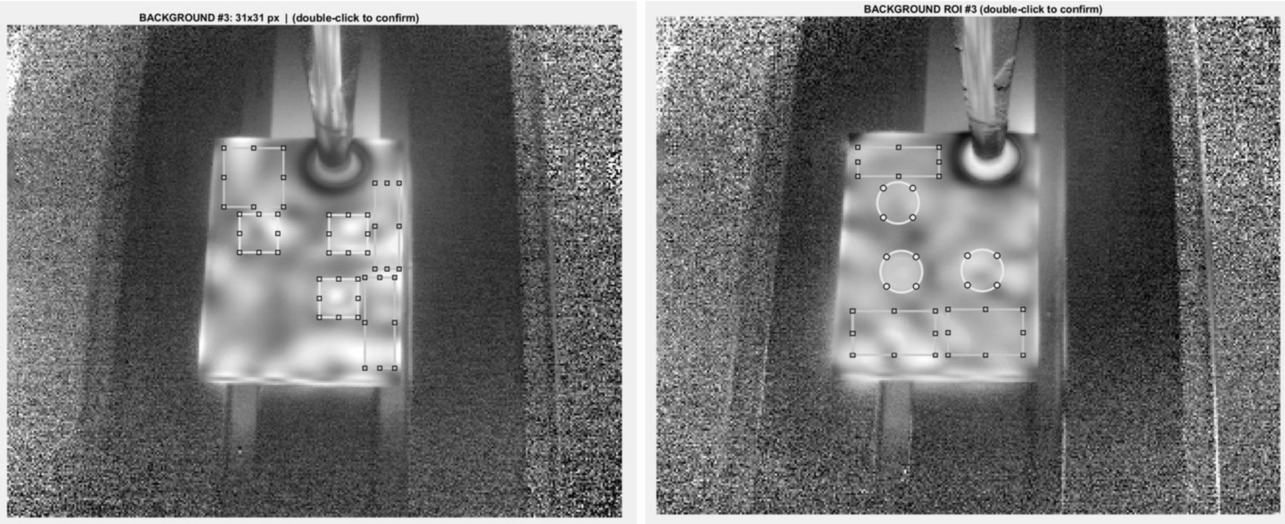

Fig. 11 *Interactive selection of ROIs for the defect zone and for the background for both defect geometries*

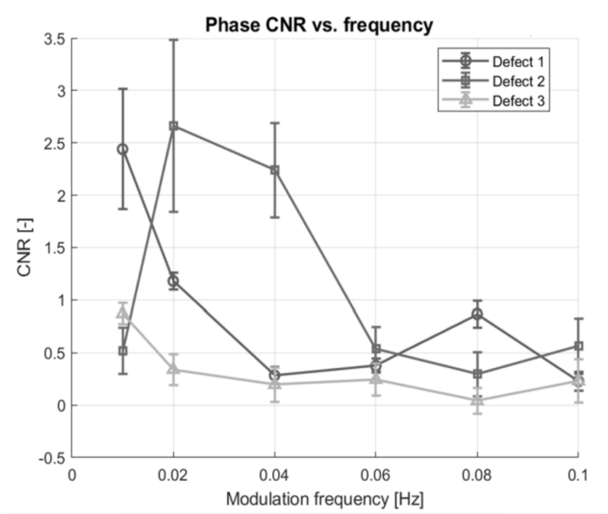

Fig. 12 *CNR values for the specimen with a square-shaped defects*

Defect 1, positioned closest to the surface, exhibited the highest CNR value at 0.01 Hz, indicating the strongest contrast at this frequency. However, at such a low frequency, the effect of thermal diffusion becomes dominant, which causes blurring of the defect edges and reduces the sharpness of its contours. The error bar for this frequency is relatively large, suggesting that the calculated CNR value was strongly influenced by the selection of the background ROI. A secondary peak was observed at 0.08 Hz, which appears to be the most suitable frequency for reliably visualizing defects located at this depth.

Defect 2, located 1.5 mm below the surface, reached its maximum CNR values at 0.02 and 0.04 Hz. At 0.02 Hz, however, the result again showed a strong dependence on the background position (as reflected by the large error bar), while the value at 0.04 Hz can be considered more reliable. Thus, 0.04 Hz was determined to be the optimal frequency for detecting this defect.

Defect 3, situated 2 mm below the surface, was generally poorly detectable at all tested frequencies, with only a slight improvement at 0.01 Hz. This result is in good agreement with visual inspection, where the defect was only weakly visible across the frequency spectrum.

Figure 13 presents the results of the CNR evaluation for circular defects at different depths. In comparison with square-shaped defects, the CNR values did not reach similarly high levels, which indicates that circular defects were generally less detectable due to their geometry.

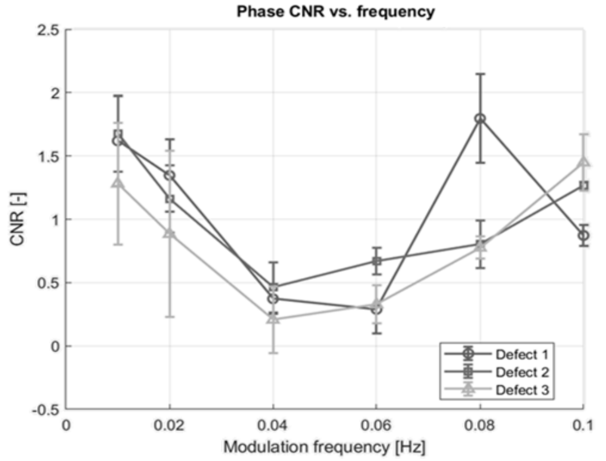

Fig. 13 *CNR values for the specimen with circular-shaped defects*

Defect 1, located closest to the surface (1 mm beneath it), exhibited its maximum CNR value at 0.08 Hz. This observation is consistent with the theoretical relation between modulation frequency and thermal diffusion length (Eq. 5), where higher frequencies are more suitable for near-surface defects. At lower frequencies (0.01 Hz), the contrast was also relatively high, but the edges of the defect became blurred due to thermal diffusion, leading to a less precise definition of its shape.

Defect 2 (located 1.5 mm beneath the surface) and Defect 3 (located 2 mm beneath the surface) both reached their highest CNR values at 0.01 Hz, which corresponds to deeper thermal wave penetration. Nevertheless, the magnitude of these values remained relatively low compared to the square-shaped defects, and the large error bars again suggest that the visibility of circular defects is highly dependent on background selection.

7 Conclusion

The conducted experiments demonstrated that several factors significantly influence the detectability of subsurface defects in Onyx composite specimens using ultrasonic-excited infrared thermography. First, the position of the ultrasonic sonotrode was shown to strongly affect the results. Placement at the edge of the specimen enhanced defect visibility due to multiple reflections and constructive wave superposition, whereas positioning in the center produced weaker responses.

The geometry of the defects was also found to play a decisive role. Square-shaped defects consistently exhibited higher CNR values than circular ones. This observation can be explained by the presence of sharp edges and corners in square geometries, which act as stress concentrators and generate more pronounced frictional heating at the defect–matrix interface.

From an excitation standpoint, it was confirmed that two excitation periods are optimal for specimens of 4 mm thickness. Increasing the number of periods led to excessive surface heating and, in some cases, sample damage.

The quantitative MATLAB CNR analysis further validated the superiority of square defects in terms of detectability, as they produced higher CNR values compared to circular ones. In both geometries, defects exhibited elevated CNR values at a modulation frequency of 0.01 Hz; however, at this frequency, the defect contours appeared blurred due to thermal wave diffusion. By contrast, higher modulation frequencies provided clearer defect boundaries but were limited to defects located closer to the surface, while lower frequencies penetrated deeper into the material and revealed defects at greater depths.

This study strictly focused on optimising the UTvis parameters for a fully dense Onyx material (100 % infill). While this approach facilitated homogeneous experimental conditions, the influence of varying infill percentages on the signal intensity and defect visibility is recognised as a highly relevant factor. This variability is planned to be the subject of our future research, which will investigate the quantitative relationship between infill density and ultrasonic response.

Overall, the detection capability of the applied ultrasonic infrared thermography method was proven effective up to approximately 2.5 mm beneath the surface. The defect positioned at a depth of 3 mm could not be detected in any of the phase thermograms, setting a practical limit for this configuration.

Acknowledgement

This research was supported by the Scientific Grant Agency VEGA under project No. 1/0753/24 and by the Cultural and Educational Grant Agency KEGA under project No. 020ŽU-4/2025 and the EU NextGenerationEU through the Recovery and Resilience Plan for Slovakia under the project No. 09I03-03-V05-00002.

References

[1] GANESAN, D., SALUNKHE, S., PANGHAL, D., MURALI, A. P., MAHALINGAM, S., TARIGONDA, H., GAWADE, S. R, HUSSEIN, M. A. (2023). Optimization of Abrasive Water Jet Machining Process Parameters on Onyx Composite Followed by Additive Manufacturing. In: *Processes*, Vol. 11, Issue 8, No. 2263. DOI: 10.3390/pr11082263

[2] HE, Q., MAN, Z., CHANG, L., YE, L. (2020). On structure-mechanical and tribological property relationships of additive manufactured continuous carbon fiber/polymer composites. In: *Structure and Properties of Additive Manufactured Polymer Components*, Vol. 2, No. 359. DOI: 10.1016/B978-0-12-819535-2.00012-0

[3] NIKIEMA, D., BALLAND, P., SERGENT, A. (2023). Study of the Mechanical Properties of 3D-printed Onyx Parts: Investigation on Printing Parameters and Effect of Humidity. In: *Chinese Journal of Mechanical Engineering Additive Manufacturing Frontiers*, Vol. 2, Issue 12, No. 100075. DOI: 10.1016/j.cjmeam.2023.100075

[4] SHANMUGAM, V., BABU, K.., KANNAN, G., MENSAH, R. A., SAMANTARAY, S. K., DAS, O. (2024). The Thermal properties of FDM printed polymeric materials: A review. In: *Polymer Degradation and Stability*, Vol. 228, No. 110902. DOI: 10.1016/j.polymdegradstab.2024.110902

[5] CALDOVA, K., SKOLAKOVA, A., PINC, J., VOJTECH, D. (2025). Characterization of microstructure and defects in the Ti-6Al-4V alloy produced by 3D printing SLM

technology. In: *Manufacturing Technology*, Vol. 25, Issue 6. DOI: 10.21062/mft.2025.083

[6] FERNANDES, R.R., TAMIJANI, A.Y., AL-HAIK, M. (2021). Mechanical characterization of additively manufactured fiber-reinforced composites. In: *Aerospace Science and Technology*, Vol. 113, Issue 3, No. 106653. DOI: 10.1016/j.ast.2021.106653

[7] HUANG, J., WEI, Q., ZHOU, L., ZHU, J., LI, CH., WANG, Z. (2023). Detection and quantification of artificial delaminations in CFRP composites using ultrasonic thermography. In: *Infrared Physics & Technology,* Vol. 130, Issue 2, No. 104579. DOI: 10.1016/j.infrared.2023.104579

[8] MADAJ, R., VERES, M., KOHAR, R., WEIS, P., SULEK, F. (2025). Overcoming Rotary Mechanism Limitations in CNC Machines: A3-PRS Approach. In: *Manufacturing Technology,* Vol. 25, Issue 4. DOI: 10.21062/mft.2025.050

[9] MONTANINI, R., FRENI, F., ROSSI, G.L. (2012). Quantitative evaluation of hidden defects in cast iron components using ultrasound activated lock-in vibrothermography. In: *Rev Sci Instrum*, Vol. 83, Issue 9, No. 094902. DOI: 10.1063/1.4750977

[10] CIAMPA, F., MOHMOODI, P., PINTO, F., MEO, M. (2018). Recent Advances in Active Infrared Thermography for Non-Destructive Testing of Aerospace Components. In: *Sensors*, Vol 18, Issue 2, No. 609. DOI: doi.org/10.3390/s18020609

[11] ALEXOPOULOU, V.E., CHRISTODOULOU, I.T., MARKOPOULOS, A.P. (2024). Investigation of Printing Speed Impact on the Printing Accuracy of Fused Filament Fabrication (FFF) ABS Artefacts. In: *Manufacturing Technology*, Vol. 24, Issue 3. DOI: 10.21062/mft.2024.042

[12] METZ, CH., FRANZ, P., FISCHER, CG., WACHTENDORF, V., MAIERHOFER, CH. (2019). Active thermography for quality assurance of 3D-printed polymer structures. In: *Quantitative InfraRed Thermography Journal*, Vol 18, Issue 1, pp. 50-71. DOI: 10.1080/17686733.2019.1686896

[13] SAPIETA, M., DEKÝŠ, V., KOPAS, P., JAKUBOVIČOVÁ, L., ŠAVRNOCH, Z. (2023). The impact of Excitation Periods on the Outcome of Lock-in Thermography. In: *Materials*, Vol. 16, Issue 7, No. 2763. DOI: 10.3390/ma16072763

[14] PISONERO, J., RODRÍGUEZ-MARTÍN, M., GONZÁLEZ-AGUILERA, D., GARCÍA-MARTÍN, R. (2025). Optimization of lock-in thermography applied for automatic identification of internal defects in 3D-printing polymer. In: *Mechanics and Materials in Design*. DOI: 10.1007/s10999-025-09812-1

[15] JELINEK, M., REINHART, G. (2020). Knowledge-based approach in the field of non-destructive inspection of CFRP metal hybrid components via optical lock-in thermography. In: *NDT & E International*, Vol. 116, No. 102264. DOI: 10.1016/j.ndteint.2020.102264

[16] HIDAYAT, Z., AVDELIDIS, N.P., FERNANDES, H. (2025). Brief Review of Vibrothermography and Optical Thermography for Quantification in CFRP Material. In: *Sensors*, Vol. 25, Issue 6, No. 1847. DOI: 10.3390/s25061847

[17] TAI, J. L., SULTAN, M. T. H., LUKASZEWICZ, A., JOZWIK, J., OKSIUTA, Z., SHAHAR, F. S. (2025). Recent Trends in Non-Destructive Testing Approaches for Composite Materials: A Review of Successful Implementations. In: *Materials*, Vol. 18, Issue 13, No. 3146. DOI: 10.3390/ma18133146

[18] LOGANATHAN, T. M., SULTAN, M. T. H., AMIR, S. M. M., JAMIL, J., YUSOF, M. R., SHAH, A. U. (2021). Infrared Thermographic and Ultrasonic Inspection of Randomly-Oriented Short-Natural Fiber-Reinforced Polymeric Composites. In: *Polymeric and Composite Materials*, Vol. 7. DOI: 10.3389/fmats.2020.604459

[19] VAVILOV, V. P., KARABUTOV, A. S., CHULKOV, A.O., DERUSOVA, D. A., MOSKOVCHENKO, A., CHEREPETSKAYA, E. B., MIRONOVA, E. A. Comparative study of active infrared thermography, laser vibrometry, and laser ultrasonic techniques in application to the inspection of graphite/epoxy composite parts. In: *14th International Conference on Quantitative Infrared Thermography*. DOI: 10.21611/qirt.2018.098

[20] SWIDERSKI, W., PRACHT, M. (2016). Ultrasonic IR Thermography Detection of Defects in Multi-layered Aramide Composites. In: *Proc, of 19th World Conference on Non-Destructive Testing*. ISSN 1435-4934

[21] GAJDOSIK, T., VERES, M., GAJDAC, I., BASTOVANSKY, R. (2025). Experimental Evaluation of Vibration Responses to

Progressive Gear Damage in Planetary Gear. In: *Manufacturing Technology*, Vol. 25, Issue 4. DOI: 10.21062/mft.2025.056.

[22] MOSKOVCHENKO, A. I., ŠVANTNER, M., VAVILOV, V. P., CHULKOV, A. O. (2021). Characterizing Depth of Defect with Low Size/Depth Aspect Ratio and Low Thermal Reflection by Using Pulsed IR Thermography. In *Materials*, Vol. 14, Issue 8, No. 1886. DOI: 10.3390/ma14081886

[23] DEKÝŠ, V., ŠTALMACH, O., SOUKUP, J., SAPIETOVÁ, A., RÝCHLIKOVÁ, L. (2019). Detection of Composite damage by IRNDT using ultrasonic and optic excitation. In: *MATEC*, Vol. 254, No. 05004. DOI: 10.1051/matecconf/201925405004

[24] BREITENSTEIN, O., STURM, S. (2019). Lock-in thermography for analyzing solar cells and failure analysis in other electronic components. In: *Quantitative Infrared Thermography Journal,* Vol. 16, pp. 203-217. DOI: 10.1080/17686733.2018.1563349

[25] HONNEROVA, P., HONNER, M. (2015). Survey of emissivity measurement by radiometric methods. In: *Applied Optics,* Vol. 54, Issue 4, pp. 669-683. DOI: 10.1364/AO.54.000669

[26] IBARRA-CASTANEDO, C., GENEST, M., PIAU, J.M., GUIBERT, S., BENDADA, A., MALDAGUE, X. P. V. (2011). Active Infrared Thermography Techniques for the Nondestructive Testing of Materials. In: *Infrared Physics & Technology*, Vol. 54, Issue 5, pp. 474-481.

[27] VAVILOV, V.P. (2009). Nondestructive testing. Handbook. Vol. 5. ISBN 978-5-904270-03-2